CONEM 2022
CONGRESSO NACIONAL DE ENGENHARIA MECÂNICA
TERESINA - PI

ABCM

XI CONGRESSO NACIONAL DE ENGENHARIA MECÂNICA
DE 07 A 11 DE AGOSTO DE 2022, TERESINA-PI, BRASIL

Effect of the interception factor with the variation of the receiver's aperture area of a Scheffler concentrator

Isabel Kodama Correa de Moraes, ikcmoraes@usp.br[1]
Erick Alfred Dib, erickadib@gmail.com[1]
Flávio Augusto Sanzovo Fiorelli, fiorelli@usp.br[1]

[1]Escola Politécnica, University of São Paulo, Mechanical Engineering Department, Avenida Prof. Mello Moraes, 2231, Butantã, São Paulo - SP, Brazil, 05508-010

Abstract: *The demand for more sustainable and low-carbon energy sources and a greater efficiency of energy conversion processes has been increasing due to the depletion of fossil fuels, the increase in energy consumption, the need to reduce environmental pollution, and curb climate change. Solar energy is an alternative source with potential for growth. Due to its low density, means of concentrating energy are used to achieve higher temperatures, which expands the application fields of solar energy. In this paper, a 2 m^2 Scheffler concentrator at the equinox was studied, whose geometry corresponds to the side section of a paraboloid bounded by an elliptical frame. Scheffler concentrators are equipped with two tracking axes (daily and seasonal) and a flexible surface, which allow focus to remain in a fixed region as the solar declination and azimuth vary. The seasonal adjustment modifies the rim angles that interfere with the concentrator's aperture area and the focal image's size. The characteristics of this concentrator enable the solar beams to concentrate outside the projection of its frame, which prevents shadow formation on the reflecting surface. It belongs to the category of image-forming reflectors that collect and concentrate solar radiation on a fixed receiver for conversion to heat. To assist receiver designs that seek to avoid thermal losses and increase efficiency, the behavior of the interception factor was evaluated according to the variation of the receiver aperture area. The results also showed the seasonal variation of the concentrator aperture and focus geometry associated with optical deviations inherent to the construction process. The analysis was performed using the EES and MATLAB programs based on the numerical model and processing of data obtained from monthly experiments conducted from June to December 2021 with a target with a Lambertian property and a CMOS (complementary metal-oxide semiconductor) sensor camera, that transforms the incoming light energy from each image point into a proportional electrical signal. The diffuse surface allows the photograph of the image produced by the radiation on the target to accurately represent the reflected flux converted from the pixel readout. The camera image records gray-scale intensity levels, which represents the way in which the beams reach the receiver. The correlation between the grayscale and the corresponding irradiance at the Lambertian target is linear, thus it is possible to characterize the distribution and identify the interception factor for a given area of the measurement plane.*
Keywords: *Solar energy, Scheffler concentrator, Interception factor, Imaging, Solar receiver*

1. INTRODUCTION

The depletion of fossil fuels, increasing energy consumption and the need to reduce environmental pollution have made it necessary to use more sustainable energy sources with lower carbon emissions (Mellalou *et al.*, 2019). The efficient use of energy and the development of technologies for the use of renewable sources are important to diversify the energy matrix and make the supply base more secure (Vieira *et al.*, 2019). The use of solar energy is a challenge due to its low density (Mellalou *et al.*, 2019). However, it is possible to increase it by concentrating the energy in a smaller area, and thus obtain a sufficient amount of heat to be used in practical applications (Bajaj *et al.*, 2016). Solar concentrators are composed of reflectors or some other optical means of concentration that conduct the incident solar energy from a large collecting area to a small absorbing area (Panchal *et al.*, 2018).

Scheffler concentrators have the particularity of having a flexible reflecting surface, whose shape is changed according to seasonality to keep the focus in the same place all year round. This mechanism changes the dimensions of the focal image. For this reason, this work evaluates the seasonal variation of a 2 m^2 Scheffler concentrator image and its relationship with the interception factor in the receiver aperture positioned in the focal plane. The Scheffler concentrator was developed by the Austrian physicist Wolfgang Scheffer with the aim of achieving a quality focus through simple structures and a reduced tracking system, so that it can be built, maintained and operated without major complications and at low cost (Iodice *et al.*, 2021). This reflector is part of the image-forming concentrator set that collects and concentrates

solar radiation on a fixed receiver for conversion to heat (Mellalou *et al.*, 2019).

The reflector tracks the movement of the sun and concentrates the sun's rays on a focus that heats a receiver, from where the heat is transferred to a working fluid that can be used for a variety of purposes (Kumar *et al.*, 2017). The concentration of the radiation allows higher temperatures to be reached, which makes it possible to use Scheffler concentrators in solar cookers, for electricity generation when associated with a turbine or a Stirling engine, desalination, cremation and different fields of industrial applications (Panchal *et al.*, 2018).

The geometry of the Scheffler reflector is defined by the intersection of an inclined plane and a paraboloid, which gives rise to an elliptical frame (Mellalou *et al.*, 2019). The projection of the frame onto the horizontal plane is a circle, which corresponds to the concentrator aperture area and whose radius equals the semi-minor axis of the ellipse (Fig. 1) (Munir *et al.*, 2010). The sun's rays fall on the reflector surface perpendicular to the Earth's polar axis at the equinox and are concentrated on a focus outside the frame projection, which prevents shadow formation on the concentrator. Although the reflector must be positioned under the sun, the image can be formed in shadow, such as inside a building. The inclination of the major axis of the elliptical frame is 43.23° at the equinox and is represented by the letter α (Dib, 2021).

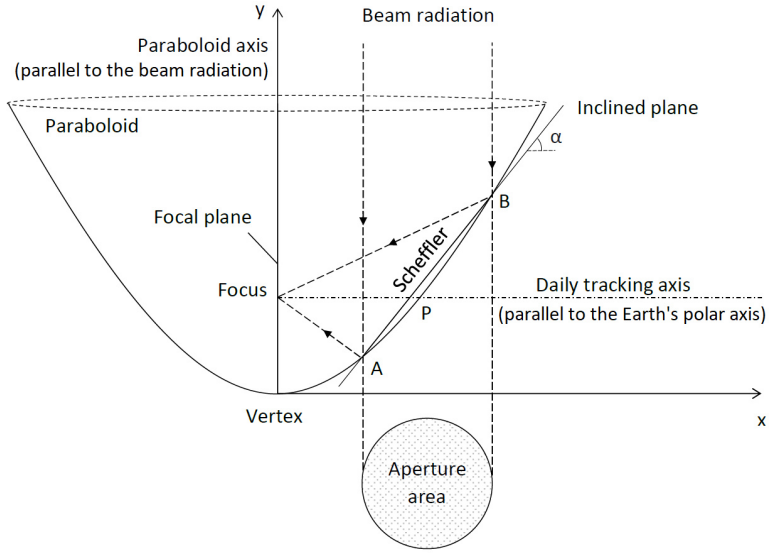

Figure 1: **Scheffler concentrator at the equinox position.**

The Scheffler concentrator has a flexible surface and two tracking axes, which allow the focus to remain in a fixed region as the solar declination as long as the azimuth change (Dib and Fiorelli, 2015). The reflecting surface follows the sun's movement throughout the day by rotating about the daily tracking axis, which has the same direction and is parallel to the Earth's polar axis. This axis passes through the focus of the paraboloid and near the center of the reflector holder, and its slope is the same as the local latitude (Shashidhar Reddy *et al.*, 2018). To annul the motion of the Earth around the sun during the day, Scheffler's dish rotates in a direction opposite to that of the Earth's rotation with a speed of 15° per hour (Indora and Kandpal, 2018).

2. SEASONAL ADJUSTMENT

The variation in the incident angle of sunlight on the Earth's surface causes the sun to be seen near the horizon line in winter and near the top of the sky in summer (Scheffler, 2006). The reflector is designed to change its slope and the shape of its surface in order to adapt to different sunlight angles and keep the focus fixed. This mechanism ensures that the focus and the concentrator remain in the same place all year round (Oelher and Scheffler, 1994).

The Scheffler concentrator can only be directed towards the north or south poles, because the orientation of the daily tracking axis is the same as the Earth polar axis. The nomenclature used in this paper was determined according to the location of the concentrator relative to the focus and is the same as that adopted by Dib (2021). A North Scheffler (NS) is positioned north of the focus and a South Scheffler (SS) south of the focus. The slope of the parabola for a given day of the year was defined by Eq. (1), where δ_n corresponds to the solar declination and ϕ to the local latitude. The positive sign refers to SS and the negative sign to NS, independent of the hemisphere in which they are located.

$$\alpha_n = 43.23^\circ \pm \frac{\delta_n}{2} - \phi \tag{1}$$

Figure 2 represents an SS at the positions of positive and negative solar declination. The axis of the paraboloid should always be parallel to the radiation beams. Adjusting the reflector inclination according to seasonality keeps the daily tracking axis and the focal plane static. The central pivot (point P) is always fixed with respect to the ground and is located near the center of the reflector. This point coincides with the seasonal tracking axis, which is perpendicular to the picture plane. The distance between P and the nominal focus (point F) is always constant (Dib and Fiorelli, 2015).

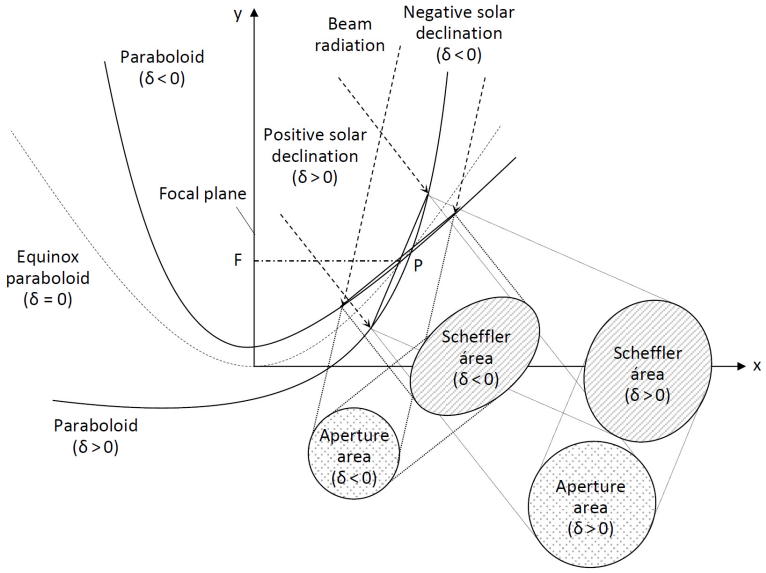

Figure 2: **Variation of the aperture area of a South Scheffler according to solar declination.**

To ensure parallelism of the paraboloid axis with the radiation beams, the paraboloid axis follows the sun's movement by rotating at an angle equal to the solar declination with respect to its position at the equinox (y-axis). The adjustment is made by tilting the major axis of the elliptical border at an angle equal to half the solar declination around P using two telescopic clamps positioned at the ends of the major axis of the reflector. The parabola's curvature closes when the major axis of the elliptical frame is stretched. As a consequence, the minor axis is contracted and the aperture area is reduced. This adjustment generates in an SS a larger aperture area at positive solar declinations than at negative solar declinations. The opposite occurs in a NS (Shashidhar Reddy and Khan, 2019).

Equation (2) expresses the solar declination with an error of less than 0.035°, where B (Eq. (3)) is a function of the day of the year ($1 \leq n \leq 365$) (Duffie and Beckman, 2013). The aperture area as a function of n is calculated by Eq. (4), where $a_{s,n}$ is the semi-minor axis of the elliptic frame (Eq. (5)) and $b_{s,n}$ the semi-major axis (Eq. (6)) (Dib, 2021).

$$\delta_n = 0.006918 - 0.399912\cos(B) + 0.070257\sin(B) - 0.006758\cos(2B) + 0.000907\sin(2B) \\ -0.002679\cos(3B) + 0.00148\sin(3B) \tag{2}$$

$$B = (n-1)\frac{360}{365} \tag{3}$$

$$A_{ap,n} = \pi \times a_{s,n} \times b_{s,n} \times cos(\alpha_n) \tag{4}$$

$$a_{s,n} = \sqrt{\frac{A_{ap,n}}{\pi}} \tag{5}$$

$$b_{s,n} = \frac{a_{s,n}}{cos(\alpha_n)} \tag{6}$$

3. IMAGE FORMATION

The process of image formation in Scheffler concentrators was based on the optical cone model demonstrated in Duffie and Beckman (2013) and the equations developed in Dib (2021) presented below. The sun was considered as a disk that projects the radiation beams onto the Earth's surface as a cone of angle $2\theta_s$ ($\theta_s \approx 4.65$ mrad $\approx 0.27°$). In an ideal concentrator, an infinitesimal area reflects the solar beams as a cone of the same opening angle. However, real concentrators have imperfections in their surface and structure, which result in an increase of $2\theta_c$ in the angle of the reflected cone. Figure 3 shows the schematic of the reflection of beams incident at points A and B viewed in the xy plane. The cone opening angle caused by the imperfections can be divided into two components (Eq. (7), one representing the deviations caused by mirrors ($2\theta_m$) and other the concentrator structure ($2\theta_b$).

$$2\theta_c = 2\theta_m + 2\theta_b \tag{7}$$

The projection of the sun onto the focal plane yz has an elliptical geometry. The beams emanating from the center of the solar disk are reflected by the entire reflecting surface and fall on F. The focal image plane has a F_y and F_z coordinate system with the origin at F. The length of a central beam is calculated by Eq. (8) according to the coordinates x_{fe}, y_{fe} and z_{fe} of the reflection point, where f is the distance between F and the origin of the coordinate system at the equinox.

$$fe = \left| \left[x_{fe}^2 + (y_{fe} - f)^2 + z_{fe}^2 \right]^{1/2} \right| \tag{8}$$

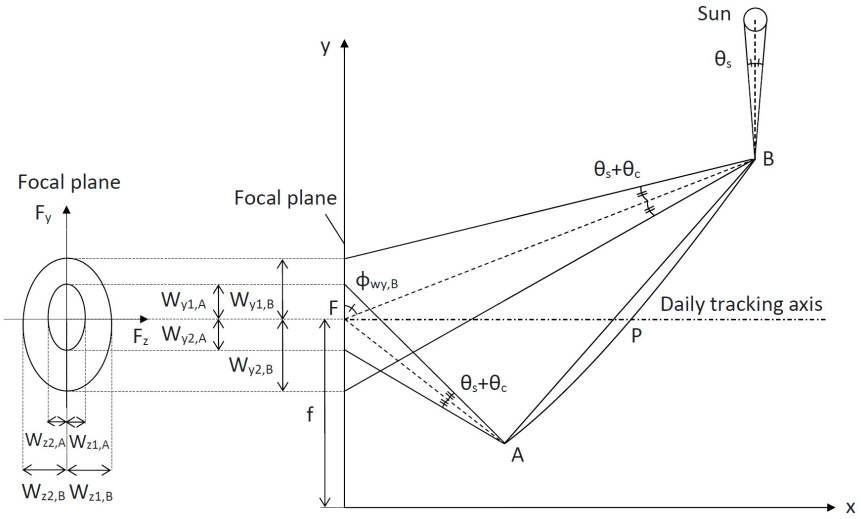

Figure 3: **Image formation of a Scheffler concentrator at the equinox.**

The image of each reflection point has four semi-axes, whose lengths are determined from Eqs. (9) to (11) according to the angles formed between the beam and the semi-axis of the image (Eqs. (12) and (13)).

$$\text{Semi-axis } w_{y1} \begin{cases} w_{y1} = fe\frac{sin(\theta_c+\theta_s)}{sin(\phi_{wy}-\theta_c-\theta_s)},\ if\ \phi_{wy} < 90° \\ w_{y1} = fe\frac{sin(\theta_c+\theta_s)}{sin(\phi_{wy}+\theta_c+\theta_s)},\ if\ \phi_{wy} > 90° \\ w_{y1} = fe \times tan(\theta_c+\theta_s),\ if\ \phi_{wy} = 90° \end{cases} \tag{9}$$

$$\text{Semi-axis } w_{y2} \begin{cases} w_{y2} = fe\frac{sin(\theta_c+\theta_s)}{sin(\phi_{wy}+\theta_c+\theta_s)},\ if\ \phi_{wy} < 90° \\ w_{y2} = fe\frac{sin(\theta_c+\theta_s)}{sin(\phi_{wy}-\theta_c-\theta_s)},\ if\ \phi_{wy} > 90° \\ w_{y2} = fe \times tan(\theta_c+\theta_s),\ if\ \phi_{wy} = 90° \end{cases} \tag{10}$$

$$\text{Semi-axles } w_z \begin{cases} w_{z1} = fe\frac{sin(\theta_c+\theta_s)}{sin(\phi_{wz}+\theta_c+\theta_s)},\ if\ \phi_{wz} < 90° \\ w_{z2} = fe\frac{sin(\theta_c+\theta_s)}{sin(\phi_{wz}-\theta_c-\theta_s)},\ if\ \phi_{wz} > 90° \\ w_z = 2 \times fe \times tan(\theta_c+\theta_s),\ if\ \phi_{wz} = 90° \end{cases} \tag{11}$$

$$cos(\phi_{wy}) = \left|\frac{y_f - y_{fe}}{fe}\right| \tag{12}$$

$$cos(\phi_{wz}) = \left|\frac{z_{fe}}{fe}\right| \tag{13}$$

4. METHODOLOGY

4.1 Indirect method

The optical characterization of a focus system is important in determining the physical characteristics of receivers (Cisneros-Cárdenas *et al.*, 2020). The solar flux distribution in the focal region was verified by the indirect measurement method. This method is widely used due to its high spatial resolution (Xia *et al.*, 2012) and is less complex than a direct measurement system that uses moving parts (Li *et al.*, 2021). The indirect method consists of capturing the irradiance distribution on a Lambertian target positioned in the focal plane with a high-resolution digital camera. The Lambertian surface reflects the same luminance in all directions within an angular range. This feature is important when the camera is positioned with an angular influence. This finish ensures that all solar radiation intercepted by the Lambertian target is detected by the camera and that the photograph accurately represents the measured flux (Ballestrín *et al.*, 2019).

The diffuse surface is obtained by a sandblasting process (Cisneros-Cárdenas *et al.*, 2020). The result of the photograph taken by the camera of the Lambertian target is a grayscale distribution of intensity levels, which represents the way in which the beams reach the receiver. However, the intensity does not correspond to the value of the incident solar

energy in physical properties. The calibration procedure is based on the possibility of relating the grayscale value of the image pixel to the corresponding irradiance value (Ballestrín *et al.*, 2019). The grayscale pixel intensity of the Lambertian surface photograph is proportional and linear to the flux at the same position (Li *et al.*, 2021).

In Ballestrín *et al.* (2019) a calibration method using a radiometer, a Lambertian target and a digital camera was presented. Validation was done by comparison with the direct measurement method that uses the radiometer on a moving plate in the measurement plane. The irradiance distributions showed a variation of 2%. The flux map of a Lambertian surface was obtained in Li *et al.* (2021) by the indirect method with a Gardon sensor. This system presented an advantage over the direct method because it is not necessary to capture several points and presents a higher spatial resolution.

Roosendaal *et al.* (2020) considered that the total power incident on the target surface is equal to the total power reflected by the reflector. Thus, the sum of the pixel intensities corresponds to the power incident on the image and can be obtained by multiplication of the effective aperture area of the reflector ($A_{ref,n}$) by the reflectivity of the mirrors (ρ_m) and the Direct Normal Irradiance (DNI), according to Eq.(14). This method was the same as Dib (2021), where the solar irradiance was measured by a pyrheliometer and used to define the gray scale (F_{gray}) and calculate the total radiation flux at the focus (Eq. (15)), where E is the pixel intensity. This procedure had an advantage because of its ease of use and generates a good estimate.

$$G_f = A_{ref,n} \times \rho_m \times DNI \tag{14}$$

$$G_f = F_{gray} \sum_{ij} E_i \tag{15}$$

The interception factor was defined as the ratio between the sums of the intensities of the pixels in the receiver aperture area and the pixels in the target surface image as shown in Eq. (16), where the indices n and N are the total number of pixels respectively in the receiver aperture area and the target surface image.

$$\gamma = \frac{\sum_i^n E_i}{\sum_i^N E_i} = \frac{\int_0^{A_{receiver}} E(y,z)\, dy\, dz}{\int_0^{A_{target}} E(y,z)\, dy\, dz} \tag{16}$$

This definition considers only the portion of the concentrated energy that intercepts the receiver aperture area and does not address aspects related to heat losses. An analysis of concentrator efficiency and sizing must consider heat exchanges of the system. Xia *et al.* (2012) verified the radiation flux distribution using an infrared camera. Solar radiation power was determined as a function of the sensor temperature response. The results showed that the interception factor increased sharply with increasing radius, until it reached a plateau when the factor approached 1 in areas of high apertures.

The analysis of the interception factor in the receiver aperture area in this paper does not require the conversion step from grayscale to power values, since it can be done by summing the pixels in each region according to Eq. (16). The pixel intensity values in each region of the focal plane are linear to its irradiance.

4.2 Experimental procedure and data processing

The experiments were conducted once a month from June to December 2021 under normal operating conditions (i.e., not controllable), at times close to solar noon and during clear skies. A CANON Rebel T6i camera with a CMOS (complementary metal-oxide semiconductor) sensor and a resolution of 6000 x 4000 pixels was used. This sensor is composed of photosensitive cells (pixels) that transform the incoming light energy from each image point into a proportional electrical signal (Ballestrín *et al.*, 2019).

The camera was positioned under the seasonal tracking axis at the height of the center pivot. A lens set at a focal length of 18 mm, three 0.9 OD neutral density filters and one 0.6 OD to 2.6 OD variable density filter were used. The filters were necessary to preserve the pixel information by avoiding its saturation due to the intensity of the luminosity reflected by the Lambertian target. The SS concentrator has a 2 m^2 aperture area at the equinox and is installed at the University of São Paulo (Fig. 4). The Lambertian target was made of carbon steel with dimensions of 1 m x 0.6 m and covered with a steel shot blasting coating and an alumina (Al_2O_2) thermal spray coating.

The photographs were taken with varying exposure times, of which one for each month of the experiment was selected for analysis. Each photograph has a particular gray scale level that is influenced by factors such as exposure time, variable density filter setting and solar irradiance at the time of the photo. The photographs were converted to grayscale and expressed in matrix form in MATLAB to allow manipulation of the data. The columns and rows of the matrix correspond to the pixel position, and the value of the elements to the intensity of the corresponding pixel.

The first step to obtain the interception factor was to isolate the energy concentration area of the photograph, which was defined as the entire region on the target where there is energy concentrated by the reflector. The sum of the pixel values contained in this region represents the total solar energy concentrated by the Scheffler reflector. Figure 5(a) is the original grayscale photograph of the Lambertian target, and Fig. 5(b) in black and white is the energy concentration area extracted from the pixel value of the photograph. It is not possible to visually observe all pixels of the concentration area in the original photograph. However, this region can be easily isolated by treating the photo as a matrix.

Figure 5(b) was represented in matrix form by assigning the value of 1 to the solar energy concentration area (white) and 0 to the rest of the matrix (black). When the matrices of the original grayscale photograph and the energy concentration

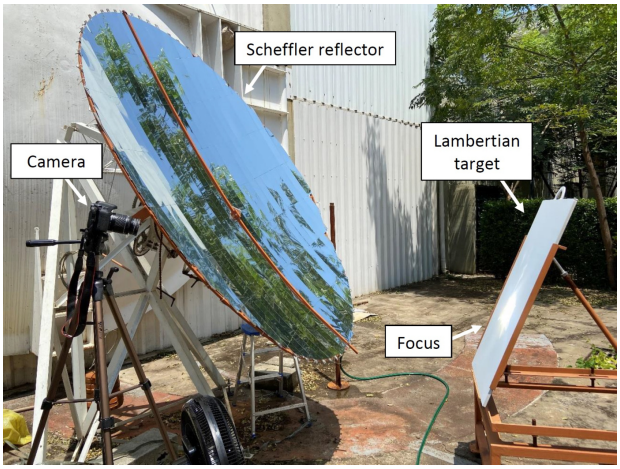

Figure 4: **Experimental set up at the University of São Paulo (23.55 S, 46.73 W).**

(a) (b)

Figure 5: **(a) Original grayscale photograph of the Lambertian target. (b) Energy concentration region in white.**

area are multiplied, the result is a matrix with non-zero values only in the focal image region. The nominal focus was considered to be the centroid of the area bounded in Fig. 5(b). Circumferences with the center at the nominal focus representing the different receiver aperture area sizes were inserted for summing the pixel intensities of the region and calculating the intercept factor. Although the theoretical focus has an elliptical geometry, a circular aperture was adopted due to ease and cost of manufacturing, similarly to what was considered in Dib (2021).

5. RESULTS AND DISCUSSION

5.1 Seasonal variation of the aperture area and image axes of a 2 m^2 South Scheffler

The first stage of the simulation consisted of evaluating the theoretical values of the concentrator aperture area and the nucleus and boundary axes for the experiment dates using the EES (Engineering Equation Solver). The nucleus was defined in this work as the smallest projection of the image generated by an infinitesimal area of the reflecting surface, while the boundary corresponds to the largest. The nucleus is the region that has the highest amount of energy per unit area, since the entire reflector contributes the flux in this region. The SS studied is composed of a reflector surface with mirrors of the MIRO-SUN® Weather-Proof Reflective 90 type, manufactured by Alanod® with anodized aluminum sheets, which generate a half-optical cone opening (θ_m) of 12.5 mrad, as reported by the manufacturer.

Figure 6(a) shows the behavior of the aperture area of an SS. The aperture area is smaller when close to the Capricorn solstice and larger when close to the Cancer solstice. In the latter case, an SS has a higher potential for capturing the incident solar irradiation because its energy catchment area is larger. Figure 6(b) shows the variations of the ellipse axes that make up the nucleus and boundary of the image when θ_b is 30 mrad. The nucleus area has a similar behavior as the aperture area (Fig. 6(c)). Its shape is more elongated on the y-axis, and the variation in z is less pronounced than in y. The variation in the dimensions of the boundary follows a different behavior. There is an interval between the Cancer solstice and the equinox, in the months of July to September, when its length in z is greater. The variation of the curve referring to the z-axis of the boundary is less pronounced on most days than the variation of the curve of its y-axis. The area of the image boundary showed a decrease between the first and second experiment and then an increasing tendency until the seventh experiment. As shown in the works of Dib and Fiorelli (2015) and Dib (2021), the behavior of the concentrator aperture area and image dimensions is cyclic and symmetric at solstices.

Equations from (9) to (11) represent the theoretical values of the image axes as a function of the deviations from the concentrator. This relation was verified by simulation in EES. The half of the reflecting surface divided by the xy-symmetry plane was arranged in a 153 x 76 matrix. Each element corresponds to a reflection point of the solar beams, at which the dimensions of the focus on the day of each experiment were calculated. The result of the matrix mirroring

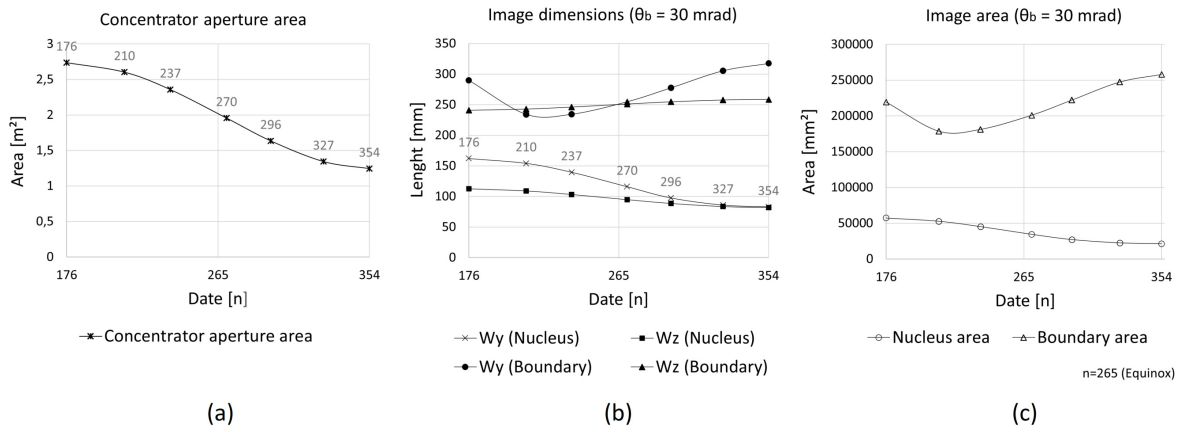

Figure 6: **(a) Aperture area of a 2 m^2 SS concentrator. (b) Variation of the seasonal image axes of an SS with $\theta_b = 30$ mrad. (c) Seasonal variation of the nucleus and boundary image area of an SS with $\theta_b = 30$ mrad. The indices indicate the dates on which the experiments were performed.**

generated data for 23,256 reflection points. In cases of real concentrators, increasing the angle of reflection raises the dimensions of the image as can be seen in the graphs in Fig. 7. For a given value of θ_b, the relationship between the image axis magnitudes for the evaluated dates is the same as in the curves of Fig. 6. The axes with the greatest variations according to seasonality show an even greater difference between each other as the angle of the optical cone increases. The variation of the image over the months for the same θ_b is due to the change in the shape of the reflecting surface characteristic of Scheffler concentrators.

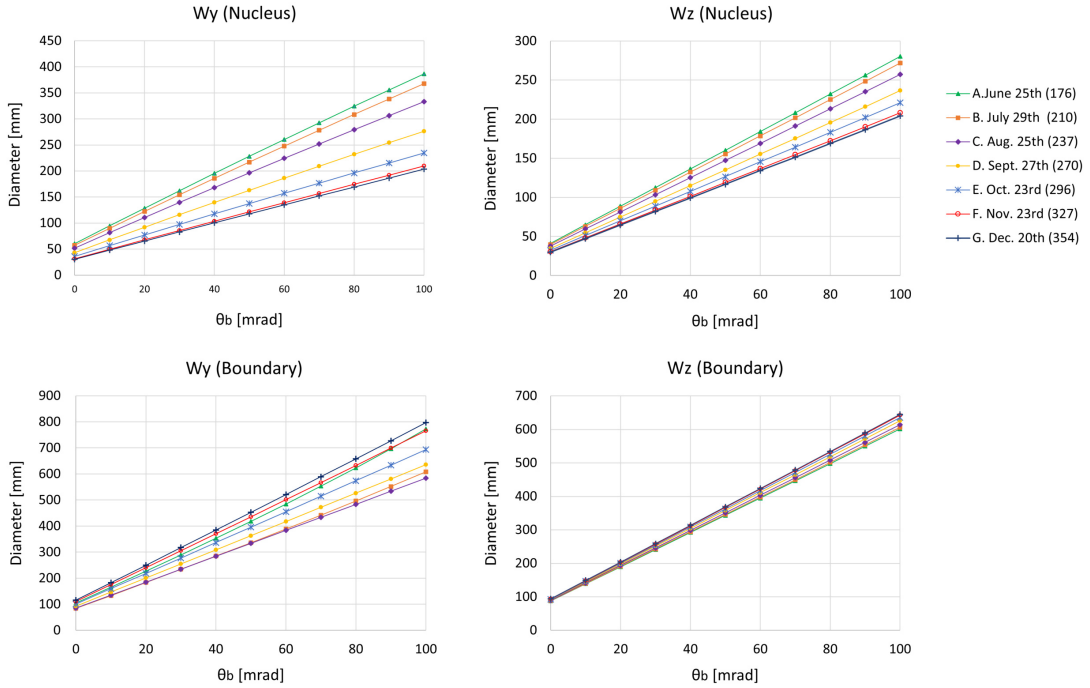

Figure 7: **Theoretical seasonal variation of the image axes with the θ_b variation.**

5.2 θ_b effect on intercept factor

The pixel value has a linear relation to the incident energy at the same location in the photograph. Figure 8(a) shows that the pixel intensity distribution has a peak at its center and a sharp drop as one moves away from it. The intercept factor analysis consisted of introducing circles of diameters up to 600 mm with their center under the centroid of the concentration area to represent the receiver aperture. The interception factor represents the proportion of the concentrated energy incident on the receiver aperture. A small concentration area tends to increase this factor for the same aperture, since all of the incident irradiation is distributed in a smaller region, i.e. it becomes more concentrated. As the receiver aperture increases, the intercept factor rises until it approaches 1 when a plateau forms, as shown in Fig. 8(b). An intercept factor equal to 1 means that all concentrated energy intercepts the receiver aperture.

For the same incident energy on the target, the increased concentration area results from more dispersed beams that

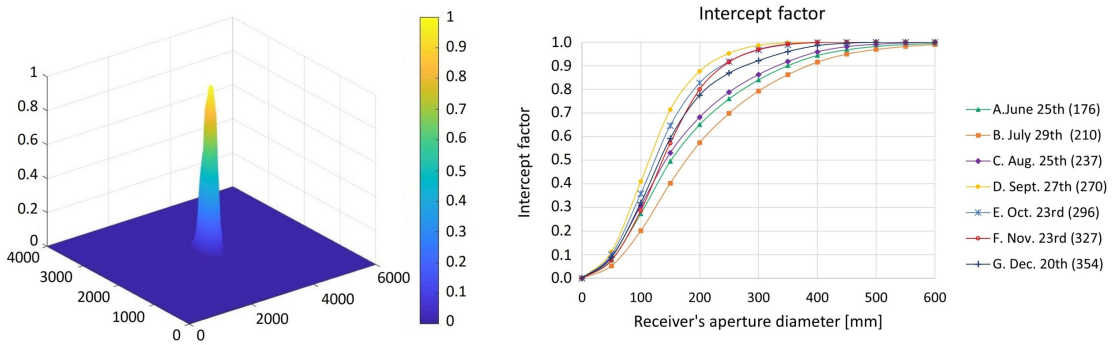

(a) (b)

Figure 8: **(a) Distribution of pixel value in the focal zone at $n = 354$. The photo resolution is 6000 x 4000 pixels. (b) Interception factor for different receiver apertures.**

generate a more uniform pixel distribution with reduced peak intensity. The increase in the concentration area is influenced by the increase in the angle of the reflection cone. The region defined as the nucleus contains the pixels of highest intensities. When its area is larger, the distribution follows the same trend of being more uniform and its peak less sharp. The growth of the intercept factor curves has been shown to be related to the area of the nucleus on each experiment date. The dates when the nuclei have larger sizes (curves E, F and G) showed a less pronounced growth of the intercept factor than the dates when the nuclei have smaller dimensions (curves A, B and C). This behavior is an indication that there is a relationship between the nucleus area and the energy flux distribution.

However, curve D does not follow this tendency, since its slope is higher than those of curves with smaller nucleus sizes. This divergence may be the result of the construction process of the concentrator. The studied concentrator was designed and built based on its position at the equinox (near the date of the curve D). When the structure of the reflector is adjusted for the equinox, the stresses and strains on the surface are smaller, which may induce smaller distortions in the geometry of the focus compared to an ideal model. The way a curve behaves can be related to the stresses originating from the manufacturing process.

The curves with less accentuated growth coincide with the periods of the year when the aperture areas of the concentrator are larger and consequently the energy capture potentials are higher. In cases of fixed aperture receivers, although the interception factors have high variations in the diameter range from 50 mm to 450 mm, it is important to verify the incident irradiations in the different periods of the year to quantify the real variations of the energy incident on the receiver apertures. Similarly, this analysis is important for receivers with variable apertures. In this case, if a single interception factor is desired, a smaller receiver aperture is required in the periods when a smaller concentrator aperture area is available. Depending on the hemisphere in which the concentrator is located, the period of greatest or smallest concentrator aperture may occur in summer or winter.

Another analysis performed consisted of evaluating the behavior of the intercept factor curve when the receiver aperture was determined from the theoretical results of the image dimensions presented in Fig. 7. In this case, the receiver aperture was considered to be circular with diameter of the same value as each of the elliptical focus axes obtained by simulation for θ_b ranging from 0 to 100 mrad. The different circumferences were inserted into the photographs of the experiments and the curves of the intercept factors were plotted as shown in Fig. 9.

It is important to emphasize that the interception factor analysis does not address processes such as heat transfers. The aperture of cavity-type receivers, for example, seeks to maximize the captured irradiance and minimize the reradiation lost within its cavity. Increasing the aperture raises both the captured and lost radiation. Therefore, both effects should be considered in more efficient receiver designs (Abuseada and Ozalp, 2020).

Since each angle is responsible for a distinct aperture diameter on each date, the curves showed a different relationship than that observed in Fig. 8(b). For a given value of θ_b, the intercept factor is compared with different aperture areas on each curve. The receiver aperture was determined according to the theoretical focus dimensions obtained from the θ_b values. The lower the opening angle of the reflected optical cone, the smaller the receiver aperture area considered in the energy interception calculation. Care should be taken when analyzing the graphs in Fig. 9, since a larger cone opening angle in the theoretical equations generates a larger aperture area considered for the pixel summation. The interpretation of these graphs cannot be confused with the idea that a higher real optical deviation generates a larger intercept factor for the same receiver aperture, since real optical deviations are associated with greater focus dispersion and reduced peak intensity. The tendency is for the interception factor to grow less sharply as the real optical deviations of the concentrator increase.

However, the graphs in Fig. 9 present the behavior of the intercept factor with respect to receiver apertures with diameters equivalent to the theoretical image axes obtained by varying the opening angle of the reflection optical cone. In the case of receiver aperture designs based on this consideration, it is interesting to see that different deflection angles should be used at each time of year to obtain an interception factor with fewer variations. Projects that use the same θ_b can generate variations greater than 30% in this factor for the case of Scheffler concentrators, which can cause high losses

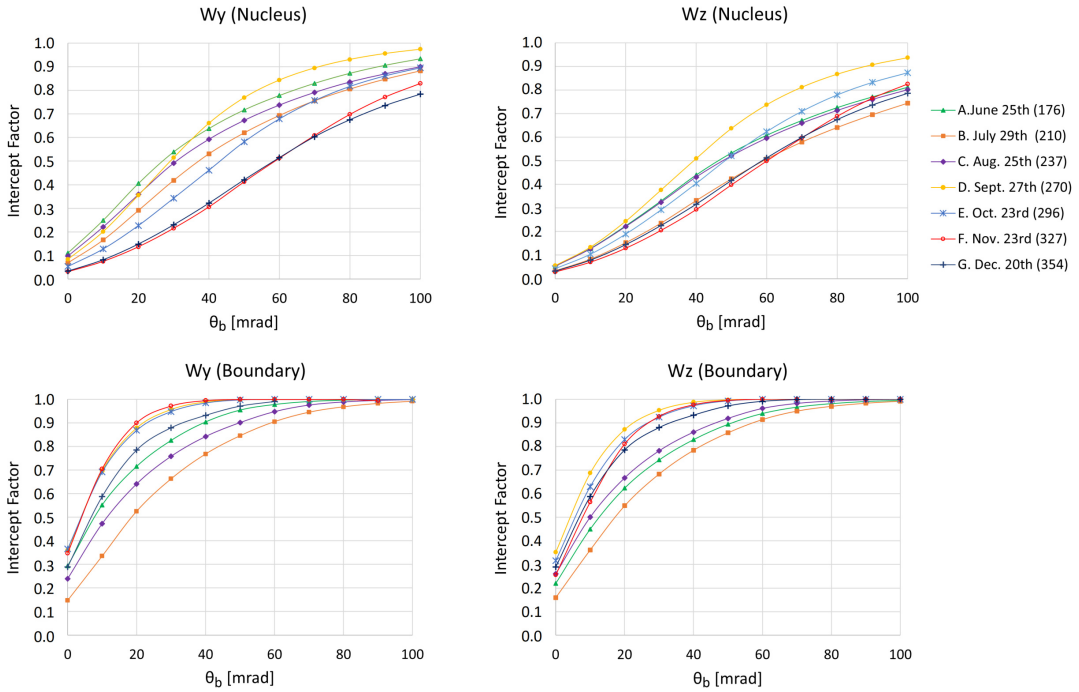

Figure 9: **Correlation between the interception factor and the theoretical dimensions obtained by varying θ_b.**

in energy capture.

6. CONCLUSIONS

Scheffler concentrators have a flexible reflective surface that changes its shape to adapt to different angles of sunlight, resulting in variations in the dimensions of its image. This paper evaluated a South Scheffler for the months of June through December 2021. The simulations showed that the concentrator's aperture area is smaller when near the Capricorn solstice and larger when near the Cancer solstice. The image was divided into the nucleus and boundary regions, both of which have elliptical geometry. The nucleus corresponds to the region where the entire reflector area contributes to the flux. Therefore, it has the highest amount of energy per unit area. The simulation showed that the nucleus is larger when near the Cancer solstice and smaller when near the Capricorn solstice. Regarding the boundary, there was a drop in area between June and July and an increasing trend until December.

A real concentrator has imperfections that raise the opening angle of the reflected optical cone by θ_b. The result is increased dimensions of the nucleus and boundary. From the experiments, a peak energy flux was observed at the center of the image and a sharp drop as it moves away from this region. Two intercept factor analyses were performed. In the first, circles from 0 to 600 mm in diameter were inserted with the center under the centroid of the energy concentration area to represent the receiver aperture. A less pronounced growth of the intercept factor was observed on the dates when the nucleus area was larger, except for the curve D near the equinox. This behavior indicates that larger nuclei have greater dispersion of the energy beams, which produces a more uniform distribution and smaller peaks. The divergence observed in curve D may come from the design and construction guidelines of the concentrator based on its position at the equinox when surface stresses and strains are lower. The curve's behavior can be related to the stresses originating from the manufacturing process. Adjustment at the equinox may induce lower distortions in the focus geometry relative to the ideal model.

The curves with lower growth coincide with the periods when the aperture area is larger and consequently there is a greater potential for energy capture. It is important to consider the incident irradiation in the different periods of the year to quantify the real variation of the energy that reaches the receiver aperture, whether fixed or variable. The second analysis of the interception factor considered that the receiver aperture diameter corresponds to the axes of the image nucleus and boundary obtained by simulation when varying θ_b from 0 to 100 mrad. Receiver designs that are based on θ_b should consider different values at each time of year if little variation in interception factor is desired. A design based on a fixed θ_b can result in variations of more than 30% in this factor, which can cause losses in energy capture. It is important to emphasize that heat transfer and solar irradiation were not considered. Both are relevant in the sizing of more efficient receivers since they are used to quantify the incident and absorbed energy by the receiver at different times of year.

7. ACKNOWLEDGEMENTS

This study was supported by the Coordenação de Aperfeiçoamento de Pessoal de Nível Superior - Brasil (CAPES) - Finance Code 001.

8. REFERENCES

Abuseada, M. and Ozalp, N., 2020. "Experimental and numerical study on a novel energy efficient variable aperture mechanism for a solar receiver". *Solar Energy*, Vol. 197, pp. 396–410. ISSN 0038-092X. doi:https://doi.org/10.1016/j.solener.2020.01.020. URL https://www.sciencedirect.com/science/article/pii/S0038092X20300220.

Bajaj, R., Raj, A. and Srinivas, T., 2016. "Mathematical modelling and analysis of variation in surface of solar scheffler concentrator for seasonal variations". In *2016 International Conference on Energy Efficient Technologies for Sustainability (ICEETS)*. IEEE, pp. 78–83.

Ballestrín, J., Casanova, M., Monterreal, R., Fernández-Reche, J., Setien, E., Rodríguez, J., Galindo, J., Barbero, J. and Batlles, F., 2019. "Simplifying the measurement of high solar irradiance on receivers. application to solar tower plants". *Renewable Energy*, Vol. 138. doi:10.1016/j.renene.2019.01.131.

Cisneros-Cárdenas, N.A., Cabanillas-López, R., Calleja-Valdez, R., Pérez Enciso, R., Pérez-Rábago, C. and García-Gutiérrez, R., 2020. "Image and ray tracing analysis of a parabolic dish collector to achieve high flux on a solar volumetric reactor". *MRS Advances*, Vol. 5, pp. 1–9. doi:10.1557/adv.2020.144.

Dib, E. and Fiorelli, F.A., 2015. "Analysis of the image produced by scheffler paraboloidal concentrator". In *2015 5th International Youth Conference on Energy (IYCE)*. IEEE, pp. 1–7.

Dib, E.A., 2021. *Análise da formação de imagem focal do concentrador solar paraboloidal tipo Scheffer*. Ph.D. thesis, Escola Politécnica, University of São Paulo, São Paulo, Brazil.

Duffie, J.A. and Beckman, W.A., 2013. *Solar Engineering of Thermal Processes*. John Wiley & Sons, Ltd., New Jersey, 4th edition.

Indora, S. and Kandpal, T.C., 2018. "Institutional cooking with solar energy: A review". *Renewable and Sustainable Energy Reviews*, Vol. 84, pp. 131–154. ISSN 1364-0321. doi:https://doi.org/10.1016/j.rser.2017.12.001. URL https://www.sciencedirect.com/science/article/pii/S1364032117315320.

Iodice, P., Amoresano, A., Langella, G. and Marra, F.S., 2021. "Combined use of volumetric expanders and Scheffler receivers to improve the efficiency of a novel direct steam solar power plant". *INTERNATIONAL JOURNAL OF ENERGY RESEARCH*. ISSN 0363-907X. doi:10.1002/er.7163.

Kumar, A., Prakash, O. and Kaviti, A., 2017. "A comprehensive review of scheffler solar collector". *Renewable and Sustainable Energy Reviews*. doi:10.1016/j.rser.2017.03.044.

Li, Q., Wang, J., Qiu, Y., Xu, M. and Wei, X., 2021. "A modified indirect flux mapping system for high-flux solar simulators". *Energy*, Vol. 235, p. 121311. ISSN 0360-5442. doi:https://doi.org/10.1016/j.energy.2021.121311. URL https://www.sciencedirect.com/science/article/pii/S0360544221015590.

Mellalou, A., Outzourhit, A., Bacaoui, A. and Qaisari, H., 2019. "Design methodologies of scheffler concentrators". In *2019 7th International Renewable and Sustainable Energy Conference (IRSEC)*. IEEE, pp. 1–4.

Munir, A., Hensel, O. and Scheffler, W., 2010. "Design principle and calculations of a scheffler fixed focus concentrator for medium temperature applications". *Solar Energy*, Vol. 84, pp. 1490–1502. doi:10.1016/j.solener.2010.05.011.

Oelher, U. and Scheffler, W., 1994. "The use of indigenous materials for solar conversion". *Solar Energy Materials and Solar Cells*, Vol. 33, No. 3, pp. 379–387. ISSN 0927-0248. doi:https://doi.org/10.1016/0927-0248(94)90239-9. URL https://www.sciencedirect.com/science/article/pii/0927024894902399.

Panchal, H., Patel, J., Parmar, K. and Patel, M., 2018. "Different applications of scheffler reflector for renewable energy: A comprehensive review". *International Journal of Ambient Energy*, Vol. 41, pp. 1–31. doi:10.1080/01430750.2018.1472655.

Roosendaal, C., Swanepoel, J. and Le Roux, W., 2020. "Performance analysis of a novel solar concentrator using lunar flux mapping techniques". *Solar Energy*, Vol. 206, pp. 200–215. doi:10.1016/j.solener.2020.05.050.

Scheffler, W., 2006. "Introduction to the revolutionary design of scheffler reflectors". *Solare Bruecke*.

Shashidhar Reddy, D. and Khan, M., 2019. "Design and ray tracing of multifaceted scheffler reflector with novel crossbars". *Solar Energy*, Vol. 185, pp. 363–373. doi:10.1016/j.solener.2019.04.083.

Shashidhar Reddy, D., Khan, M., Alam, M. and Rashid, H., 2018. "Design charts for scheffler reflector". *Solar Energy*, Vol. 163, pp. 104–112. doi:10.1016/j.solener.2018.01.081.

Vieira, B.E., Zapparoli, I.D. and Caldarelli, C.E., 2019. "Cenário energético brasileiro para o período de 2010 a 2030: Inserção de energias alternativas nos setores econômicos". *Brazilian Economic Congress (CBE)*. URL http://corecon-sc.org.br/anais-cbe2019/arquivos/anais-cbe2019-4785.pdf.

Xia, X.L., Dai, G.L. and Shuai, Y., 2012. "Experimental and numerical investigation on solar concentrating characteristics of a sixteen-dish concentrator". *International Journal of Hydrogen Energy*, Vol. 37, pp. 18694–18703. doi:10.1016/j.ijhydene.2012.09.115.

9. AUTHORSHIP RESPONSIBILITY

The authors are solely responsible for the content of this work.